The permeability of loose magma mush

Eloïse Bretagne[1*], Fabian B. Wadsworth[1], Jérémie Vasseur[2], Madeleine C. S. Humphreys[1], Donald B. Dingwell[2], Katherine J. Dobson[3], Martin F. Mangler[1], Shane M. Rooyakkers[4]

[1]Earth Sciences, Durham University, Durham DH1 3LE, U.K.

[2]Earth and Environmental Sciences, Ludwig-Maximilians-Universität, 80333 Munich, Germany.

[3] Department of Civil and Environmental Engineering, University of Strathclyde, Glasgow, UK

[4] National Isotope Centre, GNS Science, Lower Hutt 5040, New Zealand.

Models for the evolution of magma mush zones are of fundamental importance for understanding magma storage, differentiation in the crust, and melt extraction processes that prime eruptions. These models are underpinned by calculations of the permeability of the evolving crystal frameworks in the mush, which controls the rate of melt movement relative to crystals. Existing approaches for estimating the crystal framework permeability do not account for crystal shape. Here, we represent magma mush crystal frameworks as packs of hard cuboids with a range of aspect ratios, all at their maximum random packing. We use numerical fluid flow simulation tools to determine the melt fraction, specific surface area, and permeability of our 3D digital samples. We find that crystal shape exerts a first-order control on both the melt fraction at maximum packing, and on the permeability. We use these new data to generalize a Kozeny-Carman model in order to propose a simple constitutive law for the scaling between permeability and melt fraction that accounts for crystal shape in upscaled mush

This is a peer-reviewed, accepted author manuscript of the following article: Bretagne, E., Wadsworth, F. B., Vasseur, J., Humphreys, M. C. S., Dingwell, D. B., Dobson, K. J., Mangler, M. F., & Rooyakkers, S. M. (2023). The permeability of loose magma mush. Geology, 51(9), 829-832. Advance online publication. https://doi.org/10.1130/G51133.1

dynamics simulations. Our results show that magma mush permeability calculated using a model that accounts for crystal shape is significantly different compared with models that make a spherical crystal approximation, with key implications for crustal melt segregation flux and reactive flow.

Keywords: Darcy; volcanic eruption; rhyolite; magma reservoir; silicic magma

INTRODUCTION

Substantial volumes of melt are stored in magma mush regions throughout the crust (Hildreth, 1981; Sparks & Cashman, 2017). Models for the evolution of these magma mush zones are of fundamental importance for magma storage timescales, differentiation in the crust, and melt extraction processes that prime eruptions (Bachmann & Bergantz, 2004; Jackson et al. 2018). The initial assembly of crustal magma bodies requires emplacement of, and percolative reactive flow through, crystal mushes (Jackson et al. 2018). The eruption of crystal-poor magmas requires that melts be separated from these mushes (Bachmann & Bergantz, 2004). While the details of these dynamics, the controlling processes, and the overall rates, are all poorly constrained and discussed widely (Petford 2020; Holness 2018), in most models, it is the permeability of the interlocking crystal framework that is a first-order rate-limiter. Leading quantitative models for melt percolation dynamics on crystal scales use variations on a Kozeny-Carman permeability law for which the crystals are assumed to have a single radius (Petford, 1995; Bachmann & Bergantz, 2004; Jackson et al. 2018). Therefore, these constitutive models for mush permeability cannot account for crystal shape or the difference in percolative hydraulic properties between one mush and another if the phenocrysts are of similar size.

Petrological and geochronological evidence suggests that melt percolation and extraction prior to the eruption of crystal-poor rhyolites occurs in transient and episodic events rather than continuously over the thermal lifespan of the mush (e.g. Allan et al., 2013). In most known cases, the extraction timescales derived from petrological methods are rapid compared with simple gravitational compaction processes, leading to models that involve additional heat by mafic recharge magmas (e.g. Huang et al. 2015), and/or applied directional stresses and strain (Clemens & Petford, 1999; Bachmann & Bergantz 2008; Holness 2018) resulting in anisotropic dilation of the mush (Liu & Lee, 2021). Differentiating between one mechanism and another, or developing predictive frameworks for melt segregation timescales, all depend on rigorous constitutive models for the permeability of real mushes (e.g. Bachmann & Bergantz, 2004), which remains poorly investigated. A key challenge is that the 3D shape of crystals is likely to affect both the melt fraction at maximum crystal packing in the mush and the permeability at that melt fraction, such that models should seek to constrain both effects simultaneously.

METHODS: PERCOLATION OF MELTS THROUGH MAGMA MUSH

Melt extraction rates are given by the volumetric melt flux through a mush, Q, which in turn is governed by Darcy's law $\nabla P = -\mu_f Q/(kA)$ where ∇P is the driving melt pressure gradient, μ_f is the melt shear viscosity, k is the permeability of the mush, and A is the area normal to the extraction direction. Throughout we make an isotropic assumption, such that mush permeability can be treated as a pseudo-scalar and equal in all directions, in line with previous work (e.g. Bachmann & Bergantz, 2004). Previous models have used simple scaling laws for k that assume all crystals are spherical and can be defined by their radius (e.g. Bachmann & Bergantz, 2004; Huber et al. 2010; Hartung et al. 2019; Floess et al. 2019; Pistone et al. 2020). The most widely used model for k is the Kozeny-Carman equation, where k as a function of the solid volume fraction ϕ, the specific surface area of the network s, and a dimensionless constant C (c.f. Röding et al. 2020; Vasseur et al. 2021)

$$k = \frac{(1-\phi)^3}{Cs^2}. \qquad \text{Eq. 1}$$

Using the specific surface area for volumes packed with monodisperse spheres of radius R gives $s = 3(\phi)/R$, which results in $k = (1-\phi)^3 R^2/[9C(\phi)^2]$ (e.g. Hersum et al., 2015; Lui and Lee, 2021). $C = 5$ has been found to be a typical value for most granular systems (Vasseur et al. 2021; Röding et al. 2020; Torquato, 2013). However, the problem remains that the solid crystals in silicic mushes are often dominated by non-spherical crystals, and indeed may involve highly anisometric crystals such as high aspect ratio plagioclase (see Fig. 1A) or amphibole. Here, our central aim is to find a form of Eq. 1 that accounts for 3D crystal shape, and that can be used widely in mush evolution models.

We use numerical periodic domains generated by Liu et al. (2017) of packed and randomly arranged solid cuboids to approximate magma mush, which is a geometry that is closer to natural crystal shapes than spheres (c.f. Fig. 1A). Our cuboids have axis lengths a, b, and c and length aspect ratios $r_1 = c/a$ and $r_2 = b/a$. The cuboids have a square cross-section such that $a = b$ (hence, $r_2 = 1$) and the domains are produced at their random maximum packing, given by volume fraction $\phi = \phi'$ (Figure 1B). Liu et al. (2017) used order parameters to ensure that the packs are isotropic and disordered (i.e. no fabrics or cuboid preferred arrangements are found). We use a marching cubes algorithm to determine the specific surface area of each cuboid pack (Lorensen & Cline 1987), and we use LBflow – a numerical lattice-Boltzmann fluid flow simulation tool (Llewellin, 2010a, 2010b) – to characterise steady-state fluid flow through the inter-cuboid space and output the permeability of each cuboid domain (details of the numerical analysis are provided in the **Data Repository**).

RESULTS AND ANALYSIS

The results of our permeability determinations show that the permeability is a function of the melt fraction $1 - \phi$ and the specific surface area as predicted by Eq. 1, which is a function of the crystal aspect ratio r_1. All raw results are provided in the **Data Repository**. In order to analyze these results in a unified manner across a range of crystal sizes, we introduce the dimensionless permeability $\bar{k} = k/k_s = ks^2/(2\phi)$, where k_s is a generalized Stokes permeability (Vasseur & Wadsworth, 2017; Vasseur et al. 2020) and the specific surface area is measured directly for our packs. Our data for the normalized permeability $\bar{k}$ collapse to a single trend as a function of melt fraction, regardless of r_1 and crystal size (Fig. 2A), indicating that our non-dimensional approach captures these effects. In this normalized space, Eq. 1 becomes universal for any crystal shape and is $\bar{k} = (1-\phi)^3/(2C\phi)$; we find good agreement between the model and the cuboid dataset with the classic $C = 5$ (Torquato, 2013). To calibrate this further, we compare our results with published permeability data for packs of hard spheres normalized in the same way (Fig 2A). The excellent agreement we see between the numerical data and the model is used to validate Eq. 2 as a permeability model applicable to any particle/crystal shape as long as s is known. We note that in the dilute limit as $\phi \to 0$, the sphere data deviate from Eq. 1, which is explored and modeled by Vasseur et al. (2021) using a dilute expansion of k_s (see **Data Repository**).

The analysis for $\bar{k}$ relies on our determination of the specific surface area for each sample, which in turn depends on the aspect ratio r_1 and the melt fraction. In order to render this of wide utility in systems for which s is not known *a priori*, we test our model using the theoretical specific surface area of a pack cuboids with interstitial melt fraction (Eq.2; see **Data Repository** for derivation).

$$s = \frac{2\phi}{a}\left(1 + \frac{1}{r_1} + \frac{1}{r_2}\right) \qquad \text{Eq. 2}$$

which reduces to $s = 2\phi(2 + 1/r_1)/a$ when $r_2 = 1$ (square-ended cuboids used here). As with k, we can compare our results for s with the prediction of Eq. 2 across all cuboid packs used here, by making Eq. 2 scale-independent via the normalisation $\bar{s} = sa/\phi$, which reduces Eq. 2 to $\bar{s} = 4 + 2/r_1$.

We find that our data for s, converted to $\bar{s}$, collapse to a single trend, which matches the prediction of this $\bar{s}$ model (Fig. 2B). This shows that the normalized specific surface area $\bar{s}$ decreases as the cuboids move from oblate (platy-habit such that $r_1 \ll 1$) to prolate (needle-habit such that $r_1 \gg 1$), meaning that rod-like crystals have a lower specific surface area at their maximum packing. Hence, with reference to Eq. 1, the permeability of maximally packed mush consisting of prolate crystals will be higher than that of a mush made from oblate crystals. The result presented in Fig. 2B (i.e. the success of Eq. 2 in describing the specific surface area of the cuboid packs used here) suggests that the incidence of planar cuboid-cuboid contact surfaces is rare, and therefore justifies our use of Eq. 1 and the generalization of permeability by $k \propto 1/s^2$. We propose that Eq. 2 used with Eq. 1, validated herein, represents a universal model for the permeability of packs of cuboids as a proxy for the permeability of magma mush, and given in expanded dimensional form by

$$k = \frac{(1-\phi)^3 a^2}{4C\phi^2}\left(1 + \frac{1}{r_1} + \frac{1}{r_2}\right)^{-2}. \qquad \text{Eq. 3}$$

LOOSE MUSH VS MAXIMALLY PACKED MUSH

Using Eq. 3, we can calculate the permeability of percolating mush using measured or estimated crystal aspect ratios and sizes for a given melt fraction thereby accounting for crystal shape. Crystal shape not only changes the permeability at a given melt fraction, but also strongly affects the maximum packing fraction itself. Mush maximum packing fraction ϕ' is a function of r_1 (Fig. 3), and for $r_1 = 1$ (cubes), there is a local minimum in ϕ', and local maxima at $r_1 \approx 0.7$ and $r_1 \approx 1.5$. Our results are consistent with the general form for previous results for loose random packs of non-spherical particles (e.g. Donev et al. 2004; Wouterse et al. 2007; Rudge et al. 2008; Delaney et al. 2010; Meng et al. 2016; Liu et al. 2017). As crystals become highly oblate ($r_1 \ll 0.7$) or highly prolate ($r_1 \gg 1.5$), ϕ' drops, and is symmetric in $\log(r_1)$ around $r_1 = 1$. The function $\phi' = \phi'_0(Ax+1)\exp(-Bx)$ matches our data, where $\phi'_0 = 0.641$ is the numerically determined value of ϕ' at $r_1 = 1$, $x = |\log_{10}(r_1)|$, and $A = 1.26$ and $B = 1.04$ are best-fit constants.

At high melt fraction, crystals do not interact or communicate force (i.e. 'suspension'). Conversely, at the random maximum packing of crystals, a mush can support load and transmit force through the crystal framework but cannot densify further by compaction or other processes without deformation or re-organisation of the crystal framework. The transition from 'suspension' to a random maximally packed mush can be termed the ‘loose mush’ region, and we posit that the percolative extraction of melt begins when crystal fractions increase to a critical value $\phi = \phi_\tau$. We interpret ϕ_τ to be the lowest crystal volume fraction at which crystal-crystal force interactions can occur. Mueller et al., (2010) show that $\phi_\tau \approx 0.8\phi'$ for all r_1. Using this and our model for how the maximum packing varies with crystal shape, we can quantitatively define the ‘loose mush’ region. Furthermore, using our general model (Eq. 3), we can predict the permeability at ϕ_τ and ϕ' for all r_1. We note here that ϕ_τ is an approximate and indicative value, and that granular dynamics simulations demonstrate that a single melt fraction may be insufficient to demark the boundary between ‘suspension’ and ‘loose mush’ regimes (Deng et al. 2021). Regardless, whatever definition of a lower-bound on ϕ one places to demark ‘loose mush’, our model can predict k for that ϕ.

In Fig. 3 we show the results of our model (Eq. 3) in two modes of application. First, we show the general results of our permeability model for any melt fraction and a range of crystal shapes (Fig. 3; $a = 1$ mm). Second, we show the results of the model specifically for the upper and lower bounds on the ‘loose mush’ region, defined as when the crystal volume fraction is between the onset of crystal-crystal interactions, and the random maximum packing $\phi_\tau < \phi < \phi'$. This second mode of application of Eq. 3 allows us to deconvolve the two principal effects predicted here: (1) the effect of r_1 on ϕ' or ϕ_τ, and (2) the resultant effect of r_1 on the permeability. Fig. 3 shows that crystal shape can play a substantial role in controlling the absolute value of the permeability in these ‘loose’ simulated crystal mushes. A limitation of this model is that anisotropy is not considered, and that in nature, evolution of mush from ϕ_τ to ϕ' may well involve crystal rearrangements and fabric development (see Liu & Lee, 2021).

IMPLICATIONS: RATES OF PERCOLATION THROUGH MAGMA MUSH

In this study, we have used packs of square-ended cuboids, however, via Eq. 3 our model is extensible to crystals of arbitrary 3D shape. In order to apply our model to mush with real crystals, we use published data for plagioclase phenocryst shapes (Duchene et al., 2008), wherein a, b, and c are measured directly (a:b:c = 1: 6.5: 9.6; Duchêne et al. 2008). In all cases, we normalize all measured crystal shapes so that they are relative to a, which we take to be the shortest of the axes. We note that this approach does not alter r_1 and r_2. Then we assign $a = 1$ cm, in order to compute the permeabilities of mushes that comprise those shapes. Using this workflow, we find that for a given melt fraction, the permeabilities of the plagioclase mush fall within an order of magnitude of each other. Importantly, at a melt fraction of 0.5, these datasets occur at predicted permeabilities up to a maximum of 1.5 orders of magnitude greater than the prediction of the Jackson et al. (2018) scaling (Fig. 4). Since such models predict the flux of melt to the shallow crust, we posit that our model has implications for overall melt accumulation timescales. Our model (Eq. 3) can be used to predict the melt extraction rates, fluxes, and characteristic timescales, and, importantly, our results suggest that crystal shape plays a first-order role in melt extraction because the timescales λ are proportional to permeability $\lambda \propto k^{-1} \propto s^2$. Mush permeability exerts a first order control over the rates of this process, and hence crystal shape effects need to be accounted for using our model.

Acknowledgments

Funding was provided via a Durham University ‘Durham Doctoral Studentship’ (provided to Bretagne) and via both the Natural Environment Research Council (grants NE/T000430/1 and NE/M018687/2) and the European Research Council (834225 EAVESDROP). We acknowledge the authors of Liu et al. (2017) for providing their 3D digital domains. Comments from Chris Huber, Marian Holness, and an anonymous reviewer improved the manuscript substantially.

References cited

Allan, A.S.R., Morgan, D.J., Wilson, C.J.N. and Millet, M.A., 2013. From mush to eruption in centuries: assembly of the super-sized Oruanui magma body. *Contributions to Mineralogy and Petrology*, *166*(1), pp.143-164.

Bachmann, O. and Bergantz, G.W., 2008. Rhyolites and their source mushes across tectonic settings. *Journal of Petrology*, *49*(12), pp.2277-2285.

Bachmann, O. and Bergantz, G.W., 2004. On the origin of crystal-poor rhyolites: extracted from batholithic crystal mushes. *Journal of Petrology*, *45*(8), pp.1565-1582.

Clemens, J.D. and Petford, N., 1999. Granitic melt viscosity and silicic magma dynamics in contrasting tectonic settings. *Journal of the Geological Society*, *156*(6), pp.1057-1060.

Delaney, G., Cleary, P., Sinnott, M. and Morrison, R., 2010. Modelling non-spherical particle breakage in DEM simulations.

Deng, N., Wautier, A., Thiery, Y., Yin, Z.Y., Hicher, P.Y. and Nicot, F., 2021. On the attraction power of critical state in granular materials. *Journal of the Mechanics and Physics of Solids*, *149*, p.104300.

Donev, A., Cisse, I., Sachs, D., Variano, E.A., Stillinger, F.H., Connelly, R., Torquato, S. and Chaikin, P.M., 2004. Improving the density of jammed disordered packings using ellipsoids. *Science*, *303*(5660), pp.990-993.

Duchêne, S., Pupier, E., De Veslud, C.L.C. and Toplis, M.J., 2008. A 3D reconstruction of plagioclase crystals in a synthetic basalt. *American Mineralogist*, *93*(5-6), pp.893-901.

Floess, D., Caricchi, L., Simpson, G. and Wallis, S.R., 2019. Melt segregation and the architecture of magmatic reservoirs: insights from the Muroto sill (Japan). *Contributions to Mineralogy and Petrology*, *174*(4), pp.1-15.

Hartung, E., Weber, G. and Caricchi, L., 2019. The role of H2O on the extraction of melt from crystallising magmas. *Earth and Planetary Science Letters*, *508*, pp.85-96.

Hersum, T., Hilpert, M. and Marsh, B., 2005. Permeability and melt flow in simulated and natural partially molten basaltic magmas. *Earth and Planetary Science Letters*, *237*(3-4), pp.798-814.

Hildreth, W., 1981. Gradients in silicic magma chambers: implications for lithospheric magmatism. *Journal of Geophysical Research: Solid Earth*, *86*(B11), pp.10153-10192.

Holness, M.B., 2018. Melt segregation from silicic crystal mushes: a critical appraisal of possible mechanisms and their microstructural record. *Contributions to Mineralogy and Petrology*, *173*(6), pp.1-17.

Huang, H.H., Lin, F.C., Schmandt, B., Farrell, J., Smith, R.B. and Tsai, V.C., 2015. The Yellowstone magmatic system from the mantle plume to the upper crust. *Science*, *348*(6236), pp.773-776.

Huber, C., Bachmann, O. and Manga, M., 2010. Two competing effects of volatiles on heat transfer in crystal-rich magmas: thermal insulation vs defrosting. *Journal of Petrology*, *51*(4), pp.847-867.

Jackson, M.D., Blundy, J. and Sparks, R.S.J., 2018. Chemical differentiation, cold storage and remobilization of magma in the Earth's crust. *Nature*, *564*(7736), pp.405-409.

Liu, B. and Lee, C.T., 2021. Fast melt expulsion from crystal-rich mushes via induced anisotropic permeability. *Earth and Planetar*

Liu, T., Lin, B. and Yang, W., 2017. Impact of matrix–fracture interactions on coal permeability: model development and analysis. *Fuel*, *207*, pp.522-532.

Llewellin, E.W., 2010. LBflow: An extensible lattice Boltzmann framework for the simulation of geophysical flows. Part I: theory and implementation. *Computers & Geosciences*, *36*(2), pp.115-122.

Llewellin, E.W., 2010. LBflow: An extensible lattice Boltzmann framework for the simulation of geophysical flows. Part II: usage and validation. *Computers & geosciences*, *36*(2), pp.123-132.

Lorensen, W.E. and Cline, H.E., 1987. Marching cubes: A high resolution 3D surface construction algorithm. *ACM siggraph computer graphics*, *21*(4), pp.163-169.

Meng, L., Jiao, Y. and Li, S., 2016. Maximally dense random packings of spherocylinders. *Powder Technology*, *292*, pp.176-185.

Mueller, S., Llewellin, E.W. and Mader, H.M., 2010. The rheology of suspensions of solid particles. *Proceedings of the Royal Society A: Mathematical, Physical and Engineering Sciences*, *466*(2116), pp.1201-1228.

Petford, N., Koenders, M.A. and Clemens, J.D., 2020. Igneous differentiation by deformation. *Contributions to Mineralogy and Petrology*, *175*(5), pp.1-21.

Petford, N., 1995. Segregation of tonalitic-trondhjemitic melts in the continental crust: The mantle connection. *Journal of Geophysical Research: Solid Earth*, *100*(B8), pp.15735-15743.

Pistone, M., Baumgartner, L.P., Bégué, F., Jarvis, P.A., Bloch, E., Robyr, M., Müntener, O., Sisson, T.W. and Blundy, J.D., 2020. Felsic melt and gas mobilization during magma solidification: An experimental study at 1.1 kbar. *Frontiers in Earth Science*, *8*, p.175.

Röding, M., Ma, Z. and Torquato, S., 2020. Predicting permeability via statistical learning on higher-order microstructural information. *Scientific reports*, *10*(1), pp.1-17.

Rudge, J.F., Holness, M.B. and Smith, G.C., 2008. Quantitative textural analysis of packings of elongate crystals. *Contributions to Mineralogy and Petrology*, *156*(4), pp.413-429.

Sparks, R.S.J. and Cashman, K.V., 2017. Dynamic magma systems: Implications for forecasting volcanic activity. *Elements*, *13*(1), pp.35-40.

Torquato, S., 2013. *Random heterogeneous materials*. Springer

Vasseur, J. and Wadsworth, F.B., 2017. Sphere models for pore geometry and fluid permeability in heterogeneous magmas. *Bulletin of Volcanology*, *79*(11), pp.1-15.

Vasseur, J., Wadsworth, F.B. and Dingwell, D.B., 2020. Permeability of polydisperse magma foam. *Geology*, *48*(6), pp.536-540.

Vasseur, J., Wadsworth, F.B., Coumans, J.P. and Dingwell, D.B., 2021. Permeability of packs of polydisperse hard spheres. *Physical Review E*, *103*(6), p.062613.

Wouterse, A., Williams, S.R. and Philipse, A.P., 2007. Effect of particle shape on the density and microstructure of random packings. *Journal of Physics: Condensed Matter*, *19*(40), p.406215.

Zhang, B., Hu, X., Asimow, P.D., Zhang, X., Xu, J., Fan, D. and Zhou, W., 2019. Crystal size distribution of amphibole grown from hydrous basaltic melt at 0.6–2.6 GPa and 860–970 C. *American Mineralogist: Journal of Earth and Planetary Materials*, *104*(4), pp.525-535.

Figure 1. Mush texture compared with our simulated mush. (A) Ca-concentration map demonstrating the anisometric and cuboidal nature of plagioclase crystals (teal) with interstitial quartz (black) and clinopyroxene (grey; reproduced with permission from Holness et al., 2019, scalebar is 1 mm). (B) 3D visualization of a numerical cuboid pack ($r_1 = 0.2$) with the flow pattern at steady state represented in the melt phase (scalebar is 100 μm).

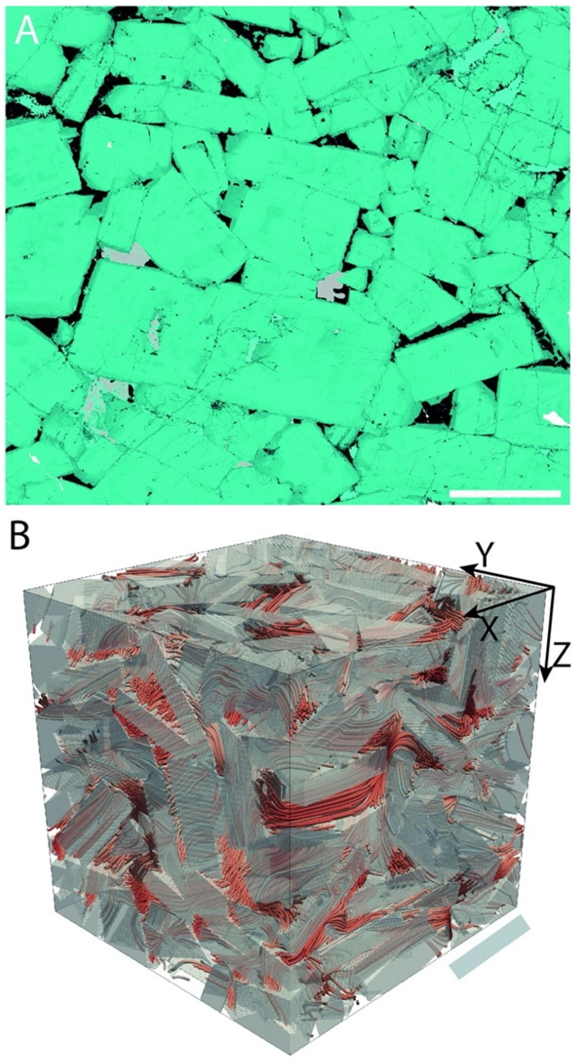

Figure 2. The permeability and specific surface area of the cuboid packs analyzed. (A) The normalised permeability k/k_s as a function of melt volume fraction $1-\phi$. The squares are the results from cuboid packs; the circles are for hard spheres (Vasseur et al. 2021) for validation and comparison. The solid curve represents our model using $C = 5$. The dashed curve is a dilute expansion for the 'suspension' regime at high melt fraction (Vasseur et al. 2021). (B) The scaling for s as a function of r_1 for cuboids cast as the normalized $\bar{s}$.

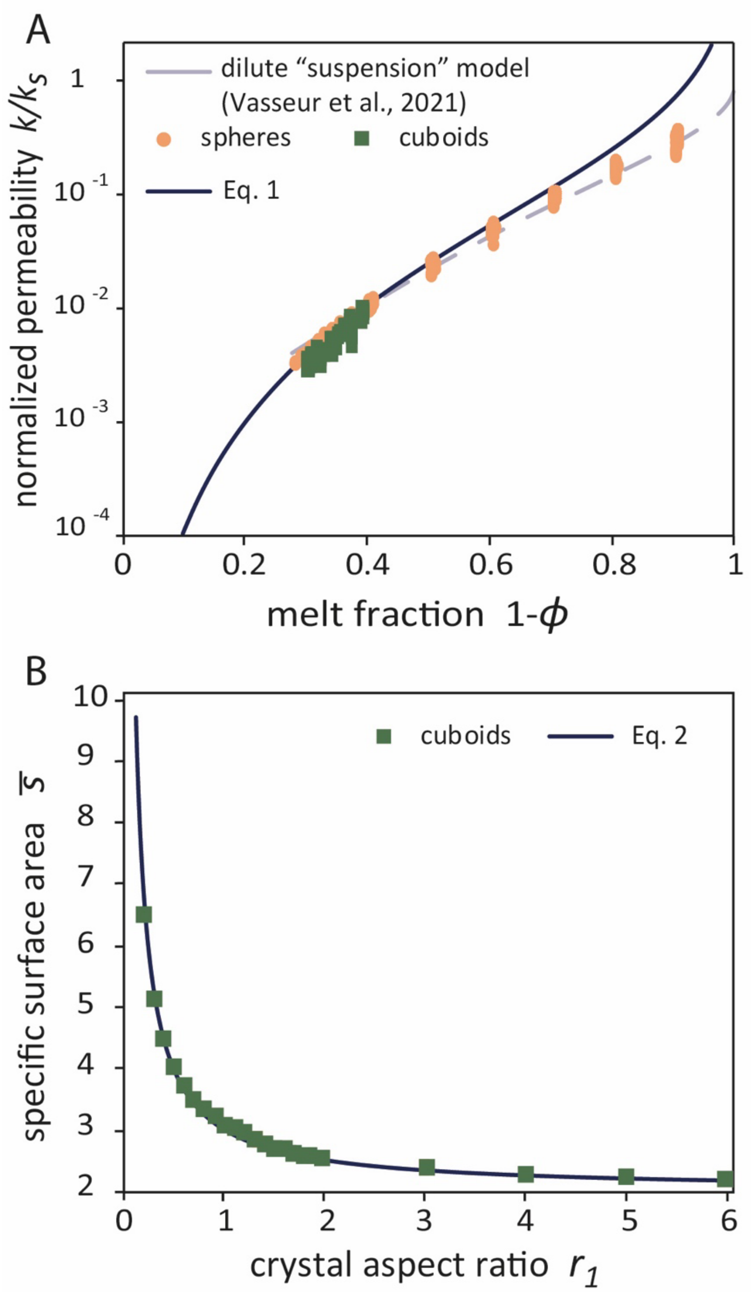

Figure 3. (A) The maximum packing crystal volume fraction ϕ' as a function of r_1 (data from Liu et al., 2017) compared with our empirical model for ϕ' (see text). The grey shaded area terminates against the upper bound of ϕ' and a lower bound at $\phi_\tau = 0.8\phi'$. (B) The model (Eq. 3) solved using $a = 1$ cm. The black curves represent the result for each aspect ratio at the specific maximum packing value (see A). The cartoons on panel A are a visual representation of the mush at different crystal fractions.

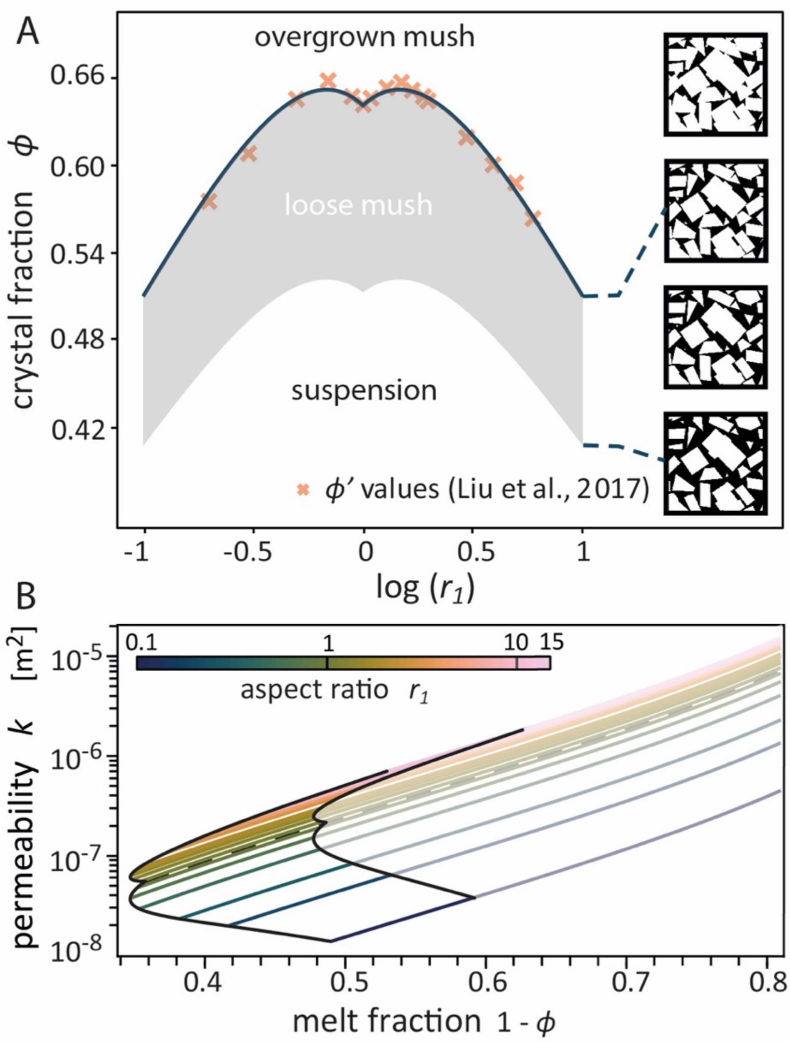

Figure 4. The model (Eq. 3) solved using input 3D crystal shapes for plagioclase (Duchene et al., 2008) phenocrysts ($a = 1$ cm). Our model is compared with the scaling from Jackson et al. (2018) $k = a^2\beta\phi^n$ where $\beta = 1/125$ and $\alpha = 3$ are the parameters proposed (Jackson et al. 2018). We also give a classical Kozeny-Carman model of the form $k = (1-\phi)^3 a^2/[150(\phi)^2]$ (e.g. Torquato 2013). Both of these comparisons underpredict plagioclase mush permeabilities given here. The vertical line at $\phi = 0.35$ is for comparison across models (Fig. 3A).